PHYSICS

Swap motion–directed twinning of nanocrystals

Qiubo Zhang[1]†, Zhigang Song[1]†, Yu Wang[1,2]†, Yifan Nie[1], Jiawei Wan[1,3], Karen C. Bustillo[4], Peter Ercius[4], Linwang Wang[1], Litao Sun[5], Haimei Zheng[1,3]*

Twinning frequently occurs in nanocrystals during various thermal, chemical, or mechanical processes. However, the nucleation and propagation mechanisms of twinning in nanocrystals remain poorly understood. Through in situ atomic resolution transmission electron microscopy observation at millisecond temporal resolution, we show the twinning in Pb individual nanocrystals via a double-layer swap motion where two adjacent atomic layers shift relative to one another. The swap motion results in twin nucleation, and it also serves as a basic unit of movement for twin propagation. Our calculations reveal that the swap motion is a phonon eigenmode of the face-centered cubic crystal structure of Pb, and it is enhanced by the quantum size effect of nanocrystals.

INTRODUCTION

Twinning is one of the most common structural transformations of materials responding to external stimuli, including mechanical loading (*1*), electron beam or ion irradiation (*2*, *3*), laser shocking (*4*), and heating (*5*). Nanocrystals with twin structures may yield superior properties, such as excellent mechanical strength (*6*), improved thermal stability (*7*), high electrical conductivity (*8*), remarkable light emission (*9*), and enhanced catalytic activity (*10*). Understanding the twinning mechanisms in nanocrystals enables the structural engineering of nanomaterials with desired properties.

Conventional wisdom holds that twinning proceeds via layer-by-layer movement of partial dislocations on adjacent atomic planes (*11*). Deformation twinning under external mechanical loading involves unconventional mechanisms, described as random activation of partial dislocation (*12*), simultaneous activation of partial dislocations (*13*), or a shuffle mechanism (*14*). Transformation twinning induced by the external stimulus other than mechanical loading is less well understood. It is assumed that the transformation twinning of nanocrystals proceeds through the traditional deformation twinning mechanism (*11*); however, this claim lacks direct evidence. Transformation twinning requires external energy to overcome the energy barrier (*2*–*5*). The injection of external energy (*15*, *16*), such as during thermal annealing and electron or ion irradiation, provides opportunities for the twin formation in nanocrystals. This indicates that the twinning of nanocrystals may exhibit nonconventional pathways controlled by kinetics. However, because the speed of partial dislocation/slip is considered to occur on time scales as fast as the speed of sound (*17*), simultaneously realizing twinning excitation and atomic imaging is still a technical challenge.

In this work, with face-centered cubic lead (Pb) nanoparticles as a model system, we investigate the transformation twinning in individual nanocrystals using transmission electron microscopy (TEM) with atomic spatial resolution and millisecond temporal resolution. Compared with other materials, Pb nanocrystals have a low melting point and are not easily oxidized, so it is ideal for driving structural transformations through controlled electron beam irradiation. To obtain a high temporal resolution, we used advanced aberration-corrected TEMs: one equipped with a Gatan K2 IS camera at 400 frames per second (fps) and the other equipped with a high-speed Thermo Fisher Scientific Ceta camera at 40 fps (*18*).

RESULTS

As shown in Fig. 1, we can observe the structure of a Pb nanocrystal as it transforms between a single crystal and a twinned crystal. The Pb nanocrystals are grown on lead titanate substrates by electron beam irradiation (figs. S1 to S4 and movie S1). They are typically in truncated octahedral shape, and a two-dimensional (2D) projection along the [01$\bar{1}$] direction is composed of four {111} and two {200} planes (Fig. 1A). On the basis of our examination of 36 nanocrystals, we determined that there are an average of 18 and 20 atomic layers in the ⟨111⟩ and ⟨200⟩ directions (Fig. 1B), respectively. During in situ imaging, the electron beam drives the structural transformation of Pb nanocrystals. Structural oscillations between the single and twinned crystals can be modulated by electron beam dose and temperature (fig. S5). We did control experiments to elucidate the origin of transformation twining in Pb nanocrystals. The results show that the formation of transformation twin is dependent on electron beam current density (fig. S5). In addition, under the same electron beam current density but at cryogenic temperature, no obvious structural fluctuations are observed (fig. S6 and movie S2). These suggest that the transformation twining arises from the enhanced thermal vibration induced by the high-energy electron beam. As shown in the representative image sequence (Fig. 1C and movie S3), a single crystal undergoing twin nucleation forms a three-layer twin embryo (0 to 0.1 s), and it propagates to become a single twin (0.1 to 0.15 s). Subsequently, the structure fluctuates between multiple parallel twins and single twins (0.15 to 0.5 s) and lastly returns to a single crystal (0.5 to 0.75 s). The corresponding fast Fourier transform (FFT) images confirm the conversion between the single and twinned crystals (Fig. 1D). The trajectory of recurrent structural transformations between the single crystal and the twinned crystal can further confirm this phenomenon (Fig. 1E). Under the electron beam illumination, the Pb particle is always in a high-energy state. Nanocrystals dissipate extra energy by phonon

[1]Materials Science Division, Lawrence Berkeley National Laboratory, Berkeley, CA 94720, USA. [2]Guangdong Provincial Key Laboratory of Functional and Intelligent Hybrid Materials and Devices, School of Molecular Science and Engineering, South China University of Technology, Guangzhou 510640, China. [3]Department of Materials Science and Engineering, University of California, Berkeley, Berkeley, CA 94720, USA. [4]National Center for Electron Microscopy, Molecular Foundry, Lawrence Berkeley National Laboratory, Berkeley, CA 94720, USA. [5]SEU-FEI Nano-Pico Center, Key Laboratory of MEMS of Ministry of Education, Collaborative Innovation Center for Micro/Nano Fabrication, Device and System, Southeast University, Nanjing 210096, China.
*Corresponding author. Email: hmzheng@lbl.gov
†These authors contributed equally to this work.

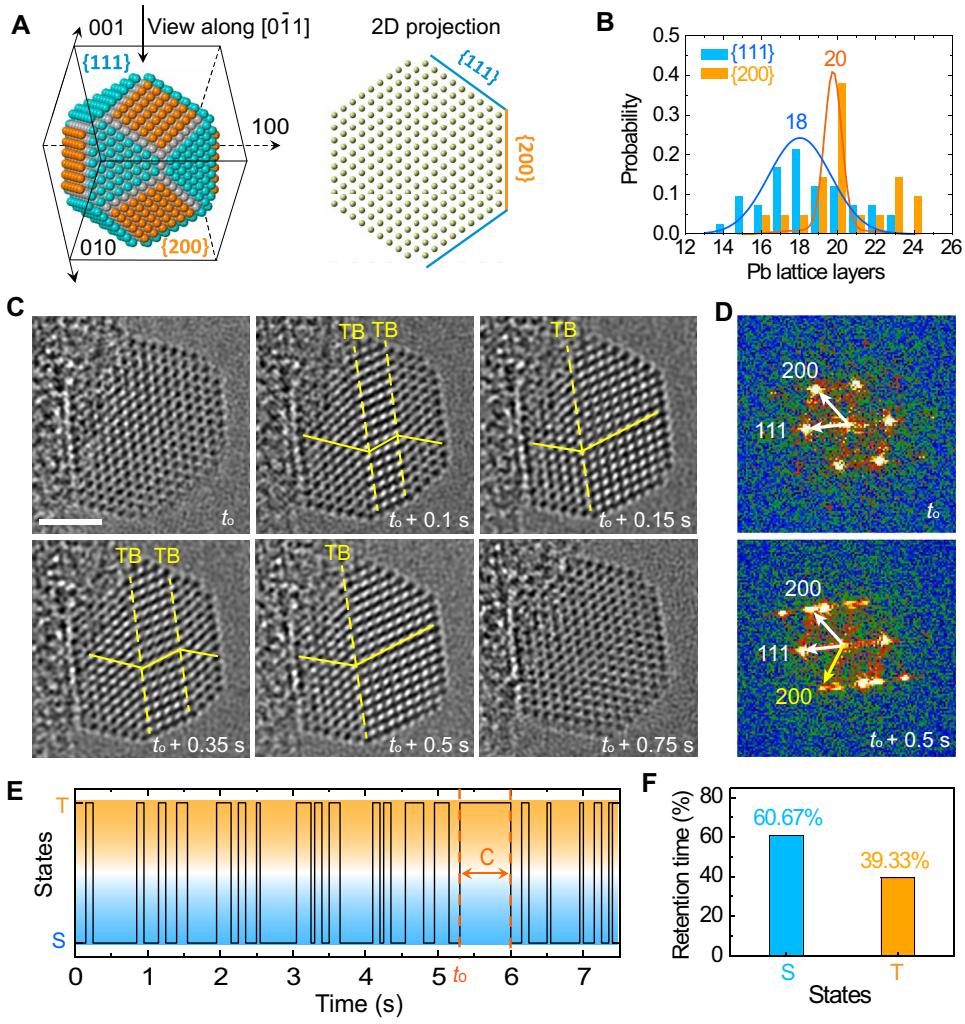

Fig. 1. Direct observation of the structural fluctuation between single-crystal and twinned structures of a Pb nanocrystal. (**A**) Reconstructed 3D atomic model of a truncated Pb nanocrystal and a two-dimensional (2D) projection along the [01$\bar{1}$] showing the view zone axis composed of four {111} and two {200} planes. (**B**) Histograms of the number of Pb layers along ⟨111⟩ and ⟨200⟩ directions as obtained from the analysis of 36 nanocrystals. (**C**) Sequential images extracted from movie S3 show the structural fluctuation between the single-crystal ("S") and twinned structures ("T") of an individual Pb nanocrystal. TB, twin boundary. Scale bar, 2 nm. (**D**) Corresponding FFT of nanostructures confirms the single-crystal and twin-crystal structural transformation. (**E**) Trajectories of structural transitions between single-crystal and nanotwin states during the twinning and detwinning process. (**F**) The retention time of single-crystal and nanotwin states in movie S3.

vibration (*19*, *20*), inducing the fluctuations between single and twinned crystals, accompanied by the nucleation and propagation of twins. The ratio of retention time of single crystal to twinned crystal is about 3 to 2 (Fig. 1F). We consider that the single crystal is more stable than the twinned crystal in terms of energetics (*21*). Thus, the single-crystal structure tends to last longer.

Figure 2 shows the atomic pathway of two-layer swap motion, which dominates the nucleation of a three-layer twin embryo (movie S4). Because of the fast speed of partial dislocation propagation and slip of two atomic layers (*17*), the nucleation of a three-layer twin embryo usually completes within one frame of our movies. To observe the atomic details of the swap motion, we use grain boundaries as obstacles to dislocation motion (*22*). Here, we focus on the highlighted red square area in Fig. 2A to study the formation of one twin embryo. We use computer vision to recognize atom positions at each frame and build ball models based on the computer-identified sites (figs. S7 to S9). They are then stacked together to visualize the atom dynamics (Fig. 2B). We found that the atomic pathway of twin nucleation is markedly different from that of deformation twinning (fig. S10) (*11*–*14*, *23*, *24*). Comparing the atom positions at 0 and 0.3 s, we show that part of the atoms in the second layer slip to the left, pinning the crystal, and a plug dislocation (dislocation pileup) formed at the movement front. The plug dislocation moves left over time. When it approaches the left end, almost all atoms in the second layer are right above the atoms in the third layer. The structure becomes unstable. In addition, the plug dislocation reaches the left end, and the second layer of atoms crosses the top of the third layer of atoms, repelling them to the right. At the final step, the second and third atomic layers move slightly to the right, adjusting themselves to form a twin embryo. At 4.1 s, some atoms fill the high-energy atom steps. These atoms are presumed to diffuse through the surface. Figure 2C shows the shift distance of each layer over time, and the

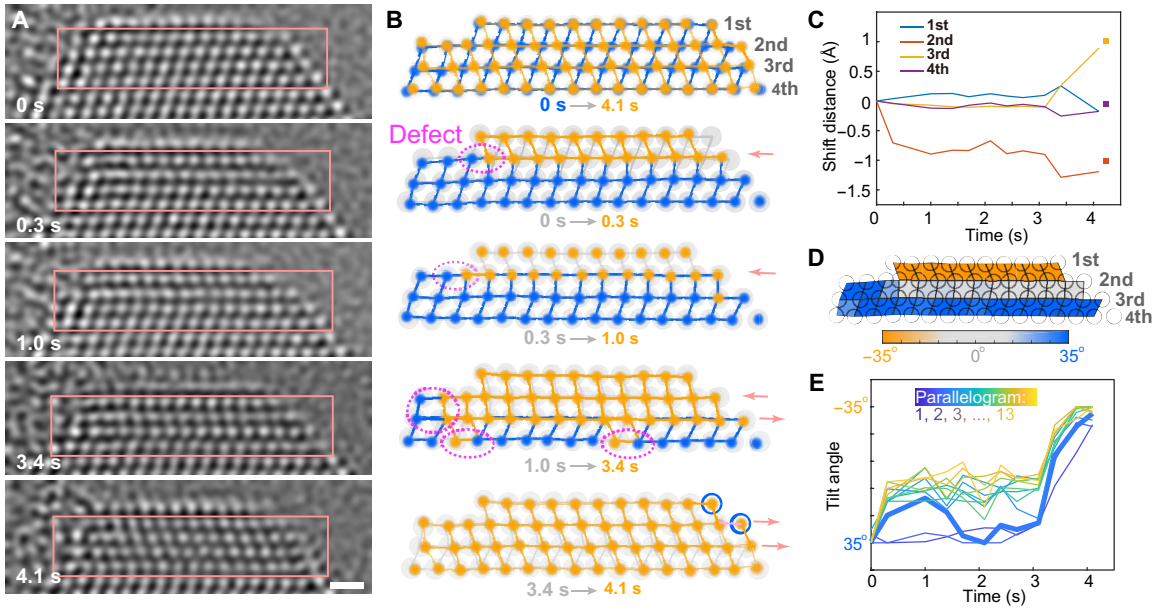

Fig. 2. Atomistic pathway of twin nucleation showing the formation of a three-layer twin embryo through swap motion. (**A**) Sequential images from movie S4 show the atomistic pathway of twinning nucleation. Scale bar, 5 Å. (**B**) The atomic positions extracted from the sequential images in (A) via computer-aided recognition show the atom movements. Each diagram compares two structures with corresponding time stamps and color labels marked around the gray arrows below. Yellow balls indicate atoms closer to the twinned structure, while blue balls are closer to the original atoms' positions. The pink arrows indicate the moving direction of the corresponding atomic layer. The purple circles mark defects. During twin nucleation, only the second and third layers of atoms move and lastly swap their vertical positions, so we call the movement swap motion. (**C**) The average shift distance of all atoms in each layer as a function of time. Positive values correspond to the right shift. (**D**) Colored diagram showing the different tilt angles of the parallelograms between adjacent atomic layers in the transition state structure at 1.0 s. Tilt angles of parallelograms are calculated from two vertical edges, and the color map shows the transition from tilting left (orange), upright (gray), to tilting right (blue). (**E**) The evolution trajectories of the tilt angles of each parallelogram between the second and third layers. Thirteen parallelograms are labeled as P1 to P13 from left to right.

small boxes show the ideal positions after twinning. Although, at 3.4 s, the first and fourth layers have slightly shifted because of internal strain, they return to the original position after structural self-adjustment at 4.1 s. From 0 to 3 s, the second layer moves to the left, and the third layer does not change. Only after the second layer crosses over the top of the third layer that the third layer starts to slide to the right (3 to 4.1 s). In summary, the second and third layers move about 1 Å in opposite directions, as if they had swapped positions, so we name it "swap motion."

From another perspective, the twinning process resembles the evolution of a phase transition. As shown in Fig. 2B, the transition state from 0.3 to 3.0 s exhibits a considerable difference in local phase states. We evaluate the local phase by analyzing the shape of the parallelograms formed by four adjacent atoms. For instance, Fig. 2D shows the quantitative color map of the tilt angles of all parallelograms at 0.3 s. Tilt angles of parallelograms are calculated from two vertical edges (average value). Although the second-layer atom only shifted left by 0.7 Å from 0 to 0.3 s, it already changes the local phase state of first- and second-layer atoms from right tilt to left tilt and causes the characteristic square phase of second- and third-layer atoms. The shape evolution of the second-row parallelograms in Fig. 2D (corresponding to second- and third-layer atoms) is critical for the twinning process. The change in tilt angle over time is shown in Fig. 2E. Note that the tilt angle of the third parallelogram (from left to right) fluctuates between 35° and 10°, reflecting the resistance to swap motion from a local defect. Once overcoming the plug dislocation, all parallelograms slip to left tilt in the time between frames from either right-tilt (P1 to P3) or square (P4 to P13). The statistical results show that most twinning nucleation proceeds through this swap motion (fig. S11).

The swap motion not only dominates the twinning nucleation but also serves as a basic unit of movement for the propagation of twinning. Some atom layers are blurred, indicating that atoms moved during single-frame acquisition, as shown by TEM simulation (figs. S12 to S14). Figure 3 suggests that a single crystal can form twins of any layers through swap motion and partial dislocation slipping units. In Fig. 3, A and B are two basic movement units. For the swap motion (Fig. 3A), the two mobile layers slip $1/6[11\bar{2}]$ along opposite directions. For the partial dislocation motion (Fig. 3B), all layers above the slip plane slip with a Burgers vector of $1/6[11\bar{2}]$. For face-centered cubic crystals, the unit cell has three atomic layers in the [111] direction. We can divide nanotwins into three categories based on the remainder of the number of layers divided by 3. If the remainder is 2, then the twinning can be completed by multiple swap motions (at least one), one of which occurs at the edge (Fig. 3C and figs. S15 and S16). As more swap motions happen in the middle of the nanoparticle, the 2-layer twin can transform into twins with $2 + 3*X$ layers (X is an integer greater than 0). If the remainder is 0, all swap motions to achieve twinning occur in the middle (Fig. 3D and figs. S17 and S18). As more swap motions happen, the 3-layer twin can become twins with $3 + 3*X$ layers (fig. S18). If the remainder is 1, for example, it forms a four-layer twin, except for one step of swap motion, then a partial dislocation slipping motion is also needed (Fig. 3E and fig. S19). With more swap motions occurring in the middle, the 4-layer twin can turn into twins with $4 + 3*X$ layers. Table S1 demonstrates a comprehensive road map for twin formation.

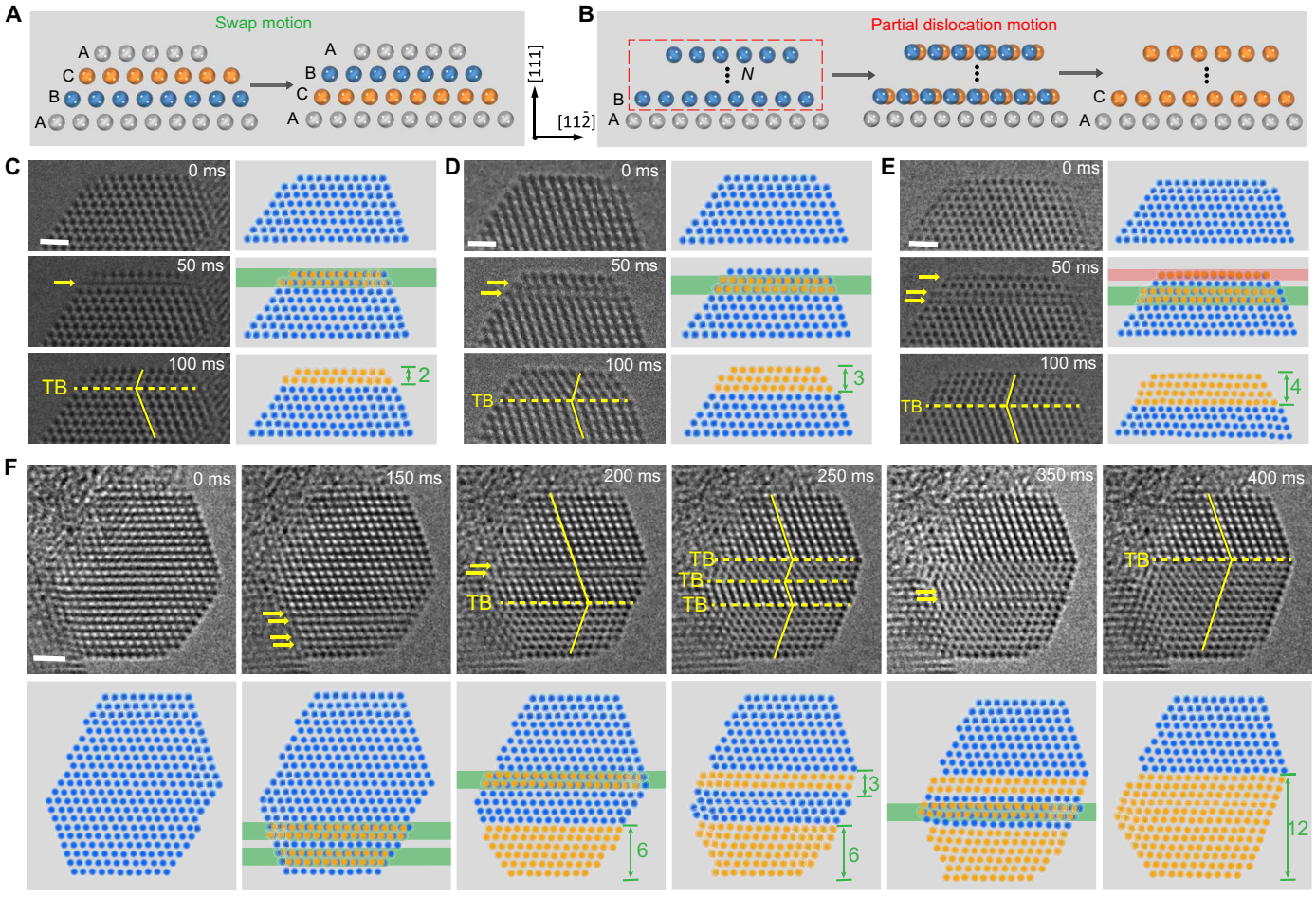

Fig. 3. The swap motion as a motion unit dominates the twin propagation. (**A**) Schematic of swap motion shows that only two adjacent atomic layers slide and lastly swap atomic vertical positions. (**B**) Schematic of partial dislocation motion shows that N ($N \geq 1$) atomic layers glide 1/6[11$\bar{2}$] on slip plane, changing their vertical position from B to C. Through these two basic motion units, any number of layers of twins can be formed in nanocrystals. (**C**) Formation of a two-layer twin through one step of swap motion at the edge. (**D**) Formation of a three-layer twin through one step of swap motion in the middle. (**E**) Formation of a four-layer twin through one swap motion combined with one partial dislocation motion. (**F**) Formation of a 12-layer twin through four steps of swap motion (movie S5). The atom layers marked out by yellow arrows in high-resolution TEM images are blurred, indicating that these layers are moving during the frame acquisition. The yellow balls represent the atoms of the formed twin, while the blue balls are atoms of matrix. The red band indicates the atomic layer taking a step of partial dislocation motion, while the green band means the two atom layers taking one swap motion. Scale bars, 1 nm.

Here, we take the formation of a 12-layer twin as an example to show the propagation of twins (Fig. 3F and movie S5). First, a single crystal undergoes two swap motions simultaneously, forming a six-layer twin. Then, it takes another swap motion and turns into a fourfold parallel twin. In the end, the two atom layers between the 3-layer twin and the 6-layer twin swap positions result in a 12-layer twin. Note that we found that the swap motions can occur simultaneously or subsequently within a nanocrystal. In addition, the swap motion can be initiated in multiple locations within a nanocrystal to form spaced twin domains (as shown in Fig. 3F). By swap motion, the structure can transform between twins with different numbers of layers.

DISCUSSION

To further understand the dynamics, we performed phonon calculations based on density functional theory (DFT). Figure 4A shows the calculated phonon band structure of a Pb nanocrystal. Each phonon mode propagates in a certain momentum indicated by the horizontal axis and oscillates at a specific frequency (namely, energy). The phonon band structure shows a valley at point T, which implies that the phonon mode at point T is soft. The wavelength of the phonons at point T is the shortest, and it is about three atomic layers (~1 nm). Amazingly, one of the eigenmodes at the position marked by a green star in Fig. 4A is a swap mode (Fig. 4B), which indicates that the swap mode is intrinsic. Because of the quantum size effect, the long-wavelength phonons are forbidden. Only phonons whose wavelength is smaller than the diameter of nanocrystals are allowed. Thus, the size effect of nanocrystals enhances the swap modes. The diameters of our Pb nanocrystals are around 10 nm. According to previous work (*2*, *15*), electron beam irradiation can influence the sample by increasing the local thermal vibration. At a finite temperature, the density of short-wavelength low-energy phonons is very high. The probability is described by $P \propto \frac{L}{\lambda(e^{-\omega_{mk}/k_B T}-1)}$, where

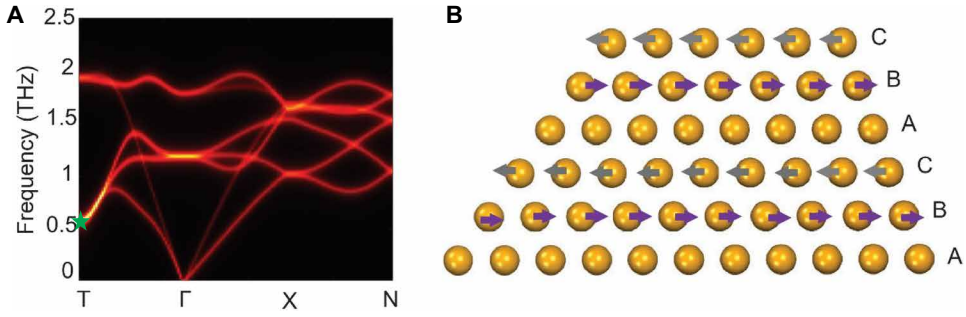

Fig. 4. Theoretical investigations of swap mode during the twinning process. (**A**) Phonon band structure of the Pb crystal. (**B**) One of the phonon eigen vibronic modes at the T point corresponds to the position marked by the green star in (A). The gray and purple arrows point out the phonon vibration directions of the adjacent atom layers.

ω_{mk} is the eigenfrequency and $\lambda = 2\pi/k$ is the phonon wavelength. T, k_B, and L are the temperature, Boltzmann constant, and characteristic size of the nanoparticles, respectively. Thus, the possibility of swap mode increases with the decrease in the nanocrystal size. Among all the short-wave phonons, the swap phonon has the lowest energy, which results in the swap mode being the most probable mode among all motion modes. Thus, the swap-model phonon may Pb to twinning due to damping. The DFT calculation is consistent with our experimental observations; the swap mode model is, in turn, physically reasonable.

In summary, our study reveals that transformation twinning of Pb nanocrystals occurs by swap motion of two adjacent atomic layers shifting relative to each other. The swap motion is responsible for the twin nucleation and twin propagation in the nanocrystals. Our findings on the previously unseen twinning mechanisms open the opportunities to develop new strategies for designing and engineering nanoscale materials.

MATERIALS AND METHODS

Experimental design: Why choose electron beam–induced twinning of nanocrystals

In these experiments, the electron beam provided the external stimuli to inject energy into the nanocrystal. Rather than heat the entire sample to induce the structural fluctuations between single-crystal and twin-crystal structures, electron beam excitation can reduce the complexity of the research system, and it is easy to control the electron beam intensity in situ. To study the twinning mechanisms of Pb nanocrystals at atomic resolution, the zone axis of the crystal must be along the [110] direction. To slow the dislocation motion central to the twinning process, we used the interface between the Pb particles and the $PbTiO_3$ substrate to block the slip movement of dislocations. No ligands were attached to the surface of the particles prepared by the in situ method, which eliminated the influence of ligands on the twinning of nanocrystals. By slowing the process and using the 1.6- to 2.5-ms cameras, we were able to obtain the data resulting from our models.

Synthesis of $PbTiO_3$ nanorods

We synthesized the PX-phase lead titanate ($PbTiO_3$) nanorods by a hydrothermal method (*25*). Typically, 4 mmol $Ti(OC_4H_9)_4$ was first dissolved in a mixed solution of 8 ml of ethanol and 8 ml of deionized H_2O. Subsequently, 20 mmol KOH, 5.2 mmol $Pb(CH_3COOH)_2{\bullet}3H_2O$, and 0.05 g of polyvinyl alcohol were added to the solution and mixed homogeneously under vigorous stirring. Then, we adjusted the volume of the final feedstock to 40 ml with deionized H_2O. The ratio of Pb/Ti in the starting materials was kept to 1.3 to ensure a complete reaction of $TiO_2{\bullet}3H_2O$ gel. Then, the solution was transferred to a Teflon-lined stainless steel autoclave, and the autoclave was sealed and heated at 200°C for 3.5 hours, after which it was allowed to cool to room temperature naturally. The products were isolated by centrifugation at 6000 rpm for 10 min and washed with deionized H_2O until a neutral pH was achieved and then washed in 10 weight % CH_3COOH aqueous solutions to remove the remnant PbO. The final pure PX-phase sample was obtained by another cycle of washing with deionized water and dried at 60°C in air. The structural characterization of as-synthesized $PbTiO_3$ nanorods (fig. S1) shows a well-defined single-crystal structure.

In situ growth of Pb nanocrystals

The as-prepared $PbTiO_3$ nanorods were dissolved in deionized H_2O to achieve a homogeneous suspension. Then, one drop of solution was cast on the Cu TEM grid and dried in air for 10 min. Pb particles were grown from the precursor compound ($PbTiO_3$) under electron beam irradiation at 300 keV in TEM (figs. S2 and S3). Because the size and nucleation density of the particles are related to the intensity of the electron beam, we studied the influence of the electron beam on the growth of Pb particles (fig. S4). We focused on a 114 nm–by–114 nm region and then irradiated the $PbTiO_3$ precursor with different intensities of electron beam for 5 min. After irradiation, we counted the size and number of particles on the surface of the nanorods (the position of the yellow dotted line). The results (fig. S4) show that the average size of particles increases with the electron beam intensity, while the number of particles first increases and then decreases. To reduce the impact of multiple twinning processes of particle growth, we chose the beam condition of 1×10^4 e^- $Å^{-2}$ s^{-1}, because under this beam condition, the particle size was stable, and the number of particles was relatively large.

Electron microscopy characterization

Most of the movies were acquired by the ThemIS (operated at 300 kV), a Thermo Fisher Scientific TEM equipped with an extreme field emission gun (X-FEG) gun, an image aberration corrector, and a high-speed FEI Ceta2 scintillator-coupled complementary metal-oxide semiconductor camera. The Ceta2 is capable of capturing 2048 × 2048 resolution images at ~40 fps. To increase the frame

rate, we also tried the electrostatic subframing system of ThemIS, which can achieve high temporal resolution as high as 1.6 ms.

Other movies were acquired by the transmission electron aberration-corrected microscope 1, a modified Thermo Fisher Scientific Titan TEM equipped with a high-brightness Schottky field-emission electron source (X-FEG), spherical- and chromatic-aberration corrector, and a Gatan K2 IS direct electron detector at the National Center for Electron Microscopy within the Molecular Foundry in Lawrence Berkeley National Laboratory. Using the direct electron detector, images of 1920 × 1792 (pixel size, 0.0203 nm) were captured every 2.5 ms. Energy-dispersive x-ray spectroscopy (EDS) data were acquired by the ThemIS equipped with a high-angle annular dark-field detector and four EDS detectors.

Methods to differentiate twinning via conventional or swap motion paths

For the two-layer twin formation (fig. S20), the top two layers first slip together by $\frac{1}{6}[11\bar{2}]$, and then, the first layer shifts $\frac{1}{6}[11\bar{2}]$ in the classical pathway.Thus, in the TEM image, either the top two layers or the first layer is blurred due to the fast movement. In addition, it is impossible that only the second layer is blurred. However, in the swap pathway, the two atomic layers can move successively or simultaneously, so it is possible that only the second layer is blurred.

For the three-layer twin formation (fig. S21), the top three layers first slip by $\frac{1}{6}[11\bar{2}]$, then the top two layers shift $\frac{1}{6}[11\bar{2}]$,and, lastly, the first layer shifts $\frac{1}{6}[11\bar{2}]$ in the classical pathway. Hence, atomic vacancy on the right side of the first layer will remain on the right side. However, in the swap pathway, the first layer does not move, and only the second atom layer and the third atom layer exchange positions. Therefore, the atomic vacancy in the first layer will transfer from the right end to the left end. Similar to the formation of two-layer twins, both the second and third layer blurring can only occur through the swap pathway.

In the same way, for the formation of four-layer twins (fig. S22), the blurring of the first, third, and fourth layers can only occur through the swap pathway. The atomic vacancy of the first layer that transferred from the right end to the left end further confirms the swap motion.

Theoretical calculation

We performed the calculation of phonon band structure and eigenmodes using the PWmat package based on a plane-wave basis set. The plane waves are cut off at 50 rydberg. SG15 pseudopotential and Perdew-Burke-Ernzerhof (PBE) exchange-correlation functional are applied. The atomic positions are fully relaxed until the force on each atom is below 0.001 eV $Å^{-1}$ T^{-1}, and then, the force constant is calculated in the finite displacement method. A supercell of 3 × 3 × 3 is applied. The phonon bands are calculated by Phonopy.

SUPPLEMENTARY MATERIALS

Supplementary material for this article is available at https://science.org/doi/10.1126/sciadv.abp9970

REFERENCES AND NOTES

1. J. Wang, Z. Zeng, C. R. Weinberger, Z. Zhang, T. Zhu, S. X. Mao, In situ atomic-scale observation of twinning-dominated deformation in nanoscale body-centred cubic tungsten. *Nat. Mater.* **14**, 594–600 (2015).
2. M. Song, N. Lu, J. Lee, E. Nakouzi, H. Wang, D. Li, Oriented attachment induces fivefold twins by forming and decomposing high-energy grain boundaries. *Science* **367**, 40–45 (2020).
3. J. Ding, S. Yang, B. Zhu, H. Liu, G. Liu, L. Zhou, Q. Zhan, F. Wan, Twins induced by high-temperature ion irradiation in body-centered cubic V-4Cr-4Ti alloy. *Scr. Mater.* **162**, 377–381 (2019).
4. C. E. Wehrenberg, D. McGonegle, C. Bolme, A. Higginbotham, A. Lazicki, H. J. Lee, B. Nagler, H. S. Park, B. A. Remington, R. E. Rudd, M. Sliwa, M. Suggit, D. Swift, F. Tavella, L. Zepeda-Ruiz, J. S. Wark, In situ x-ray diffraction measurement of shock-wave-driven twinning and lattice dynamics. *Nature* **550**, 496–499 (2017).
5. Y. Wang, H. C. Peng, J. Liu, C. Z. Huang, Y. Xia, Use of reduction rate as a quantitative knob for controlling the twin structure and shape of palladium nanocrystals. *Nano Lett.* **15**, 1445–1450 (2015).
6. S. Zhao, R. Zhang, Q. Yu, J. Ell, R. O. Ritchie, A. M. Minor, Cryoforged nanotwinned titanium with ultrahigh strength and ductility. *Science* **373**, 1363–1368 (2021).
7. Q. Huang, D. Yu, B. Xu, W. Hu, Y. Ma, Y. Wang, Z. Zhao, B. Wen, J. He, Z. Liu, Y. Tian, Nanotwinned diamond with unprecedented hardness and stability. *Nature* **510**, 250–253 (2014).
8. L. Lu, Y. Shen, X. Chen, L. Qian, K. Lu, Ultrahigh strength and high electrical conductivity in copper. *Science* **304**, 422–426 (2004).
9. B. Pietrobon, V. Kitaev, Photochemical synthesis of monodisperse size-controlled silver decahedral nanoparticles and their remarkable optical properties. *Chem. Mater.* **20**, 5186–5190 (2008).
10. W. Huang, A. C. Johnston-Peck, T. Wolter, W. D. Yang, L. Xu, J. Oh, C. Z. Benjamin, A. Reeve, M. E. Holtz, A. A. Herzing, M. M. Aaron, M. Lindenberg, M. Cargnello, Steam-created grain boundaries for methane C–H activation in palladium catalysts. *Science* **373**, 1518–1523 (2021).
11. J. A. Venables, Deformation twinning in face-centred cubic metals. *Philos. Mag.* **6**, 379–396 (1961).
12. X. L. Wu, X. Z. Liao, S. G. Srinivasan, F. Zhou, E. J. Lavernia, R. Z. Valiev, Y. T. Zhu, New deformation twinning mechanism generates zero macroscopic strain in nanocrystalline metals. *Phys. Rev. Lett.* **100**, 095701 (2008).
13. B. Q. Li, B. Li, Y. B. Wang, M. L. Sui, E. Ma, Twinning mechanism via synchronized activation of partial dislocations in face-centered-cubic materials. *Scr. Mater.* **64**, 852–855 (2011).
14. B. Li, E. Ma, Atomic shuffling dominated mechanism for deformation twinning in magnesium. *Phys. Rev. Lett.* **103**, 035503 (2009).
15. H. Zheng, J. B. Rivest, T. A. Miller, B. Sadtler, A. Lindenberg, L.-W. Wang, M. F. Toney, C. Kisielowski, A. P. Alivisatos, Observation of transient structural-transformation dynamics in a Cu_2S nanorod. *Science* **333**, 206–209 (2011).
16. S. Jeon, T. Heo, S. Hwang, J. Ciston, K. C. Bustillo, J. H. Bryan, W. Reed, S. Kang, S. Kim, J. Lim, K. Lim, J. S. Kim, R. S. Bloom, M. Kang, S. Hong, K. Kim, A. Zettl, W. Kim, J. Park, P. Ercius, W. Lee, Reversible disorder-order transitions in atomic crystal nucleation. *Science* **371**, 498–503 (2021).
17. P. Gumbsch, H. Gao, Dislocations faster than the speed of sound. *Science* **283**, 965–968 (1999).
18. B. W. Reed, A. Moghadam, R. Bloom, S. Park, A. Monterrosa, P. Price, C. Barr, S. Briggs, K. Hattar, J. McKeown, D. J. Masiel, Electrostatic subframing and compressive-sensing video in transmission electron microscopy. *Struct. Dyn.* **6**, 054303 (2019).
19. L. Wang, P. Guan, J. Teng, P. Liu, D. Chen, W. Xie, D. Kong, S. Zhang, T. Zhu, Z. Zhang, E. Ma, M. Chen, X. Han, New twinning route in face-centered cubic nanocrystalline metals. *Nat. Commun.* **8**, 2142 (2017).
20. D. Bozyigit, N. Yazdani, M. Yarema, O. Yarema, W. M. Lin, S. Volk, K. Vuttivorakulchai, M. Luisier, F. Juranyi, V. Wood, Soft surfaces of nanomaterials enable strong phonon interactions. *Nature* **531**, 618–622 (2016).
21. J. Wang, Z. Zeng, M. Wen, Q. Wang, D. Chen, Y. Zhang, H. Wang, P. Wang, Z. Zhang, S. X. Mao, T. Zhu, Anti-twinning in nanoscale tungsten. *Sci. Adv.* **6**, eaay2792 (2020).
22. T. Britton, D. Randman, A. Wilkinson, Nanoindentation study of slip transfer phenomenon at grain boundaries. *J. Mater. Res.* **24**, 607–615 (2009).
23. S. Mahajan, C. S. Pande, M. A. Iman, B. B. Rath, Formation of annealing twins in f.c.c. crystals. *Acta. Mater.* **45**, 2633–2638 (1997).
24. L. Liu, J. Wang, S. K. Gong, S. X. Mao, High resolution transmission electron microscope observation of zero-strain deformation twinning mechanisms in Ag. *Phys. Rev. Lett.* **106**, 175504 (2011).
25. J. Wang, K. Schenk, A. Carvalho, B. Wylie-Van Eerd, J. Trodahl, C. S. Sandu, M. Bonin, I. Gregora, Z. He, T. Yamada, H. Funakubo, P. R. Briddon, N. Setter, Structure determination and compositional modification of body-centered tetragonal px-phase lead titanate. *Chem. Mater.* **23**, 2529–2535 (2011).
26. E. J. Kirkland, *Advanced Computing in Electron Microscopy* (Springer, 1998), vol. 12.
27. R. F. Egerton, P. Li, M. Malac, Radiation damage in the TEM and SEM. *Micron* **35**, 399–409 (2004).
28. D. J. Smith, A. K. Petford-Long, L. R. Wallenberg, J. O. Bovin, Dynamic atomic-level rearrangements in small gold particles. *Science* **233**, 872–875 (1986).
29. S. B. Fisher, On the temperature rise in electron irradiated foils. *Radiat. Eff.* **5**, 239–243 (1970).
30. I. Jenčič, M. W. Bench, I. M. Robertson, M. A. Kirk, Electron-beam-induced crystallization of isolated amorphous regions in Si, Ge, GaP, and GaAs. *J. Appl. Phys.* **78**, 974–982 (1995).

31. D. B. Williams, C. B. Carter, in *Transmission electron microscopy* (Springer, 1996), pp. 3–17.
32. A. Roy, Estimates of the thermal conductivity and the thermoelectric properties of $PbTiO_3$ from first principles. *Phys. Rev. B.* **93**, 100101 (2016).
33. T. Zhu, J. Li, K. J. Van Vliet, S. Ogata, S. Yip, S. Suresh, Predictive modeling of nanoindentation-induced homogeneous dislocation nucleation in copper. *J. Mech. Phys. Solids* **52**, 691–724 (2004).
34. L. Wang, Y. Zhang, Z. Zeng, H. Zhou, J. He, P. Liu, M. Chen, J. Han, D. J. Srolovitz, J. Teng, Y. Guo, G. Yang, D. Kong, E. Ma, Y. Hu, B. Yin, X. Huang, Z. Zhang, T. Zhu, X. Han, Tracking the sliding of grain boundaries at the atomic scale. *Science* **375**, 1261–1265 (2022).

Acknowledgments
Funding: This work was supported by the U.S. Department of Energy, Office of Science, Office of Basic Energy Sciences (BES), Materials Sciences and Engineering Division, under contract no. DE-AC02-05-CH11231 within the in situ TEM program (KC22ZH). Work at the Molecular Foundry of Lawrence Berkeley National Laboratory (LBNL) was supported by the U.S. Department of Energy under contract no. DE-AC02-05CH11231. **Author contributions:** Conceptualization: Q.Z. and H.Z. Methodology: Q.Z., Y.W., Z.S., Y.N., P.E., L.W., and L.S. Visualization: Q.Z., Y.W., Z.S., Y.N., and P.E. Funding acquisition: H.Z., L.W., and P.E. Project administration: H.Z. Supervision: H.Z. Writing—original draft: Q.Z., Y.W., and Z.S. Writing—review and editing: H.Z., L.S., K.C.B., P.E., and J.W. **Competing interests:** The authors declare that they have no competing interests. **Data and materials availability:** All data needed to evaluate the conclusions in the paper are present in the paper and/or the Supplementary Materials.

Submitted 11 March 2022
Accepted 22 August 2022
Published 7 October 2022
10.1126/sciadv.abp9970